

Study on thermal damage characteristics and micromechanical behavior of structures induced by spontaneous combustion of low-rank coal

Jinglei Li ^{a,b}, Haiyan Wang ^{c,*}, Haijie Yu ^{a,b}, Guobin Li ^a

^a International Navigation College, Hainan Tropical Ocean University, Sanya, 572022, China

^b Yazhou Bay Innovation Institute, Hainan Tropical Ocean University, Sanya, 572024, China

^c School of Emergency Management and Safety Engineering, China University of Mining and Technology, Beijing, 100083, China



ARTICLE INFO

Handling Editor: Huihe Qiu

Keywords:

Coal spontaneous combustion
Thermal damage
pore structure
Nuclear magnetic resonance imaging
Micromechanical behavior
Discrete element method

ABSTRACT

Thermal damage induced by coal spontaneous combustion (CSC) has a significant impact on its development. In this study, low-rank coals were heat-treated (25–500 °C). Experiments such as nuclear magnetic resonance, scanning electron microscopy, and uniaxial compression were used to visualize and quantify the evolution of pore structure and structural strength during CSC. A multi-component discrete-element model of coal thermal fracture was developed and a sensitivity analysis of the micromechanical behavior of CSC was carried out. The results showed that during CSC, the micropores in coal gradually evolved into mesopores or macropores, and the pore diameter, porosity and permeability can be increased to 5.51 μm, 21.05 % and 1.51 mD respectively with the temperature. Significant thermal damage occurred in low-rank coal at 100 °C, leading to a sharp decrease in its load-bearing capacity, which made it easier to reach the damage condition and produce more cracks. And then the thermal damage was fluctuating with the increase of temperature. From 100 °C to 500 °C, the micromechanical behavior of low-rank coal is similar, and the variation of the critical value with temperature is small. The study results can serve as a reference for controlling coal fires.

1. Introduction

Coal is a naturally complex porous organic rock, its pore system is critical for internal fluid transportation and directly determines fluid storage and transport [1,2]. When coal spontaneous combustion (CSC) occurs, there is a dramatic increase in heat within coal, accompanied by thermal expansion of the matrix, water evaporation and volatiles precipitation. As the reaction proceeds, the coal body undergoes thermal damage, increasing the permeability of the coal body. Meanwhile, the heat generated by the coal-oxygen reaction will act on the coal body again, resulting in secondary thermal damage to the coal body [3]. In the later stages of the reaction, the changes in coal body provide favorable conditions for fresh air from the outside, accelerating the combustion of coal body [4,5]. It can be seen that thermal damage induced by CSC plays a crucial role in its development.

The pore system of coal is altered under thermal conditions, which in turn affects the physical and mechanical properties of coal.

* Corresponding author. School of Emergency Management and Safety Engineering, China University of Mining and Technology, Beijing, Ding No.11 Xueyuan Rd, Haidian District, 100083, China.

E-mail address: whyhyp@163.com (H. Wang).

This thermal damage is irreversible, and coal also undergoes different thermal damage processes under different heating modes [6–8]. Currently, studies on thermal damage to coal structures are more often carried out in environments such as low-temperature oxidation and microwave drying, and the studies under high-temperature conditions have not yet matured. Even for studies in high-temperature environments, scholars have focused more on coal thermal damage of under rapid heating conditions [9], which is clearly not in accordance with the developmental process of CSC. The inhomogeneous thermal stresses generated during heating of coal can damage its internal structure. Studies have shown that under high temperature conditions, the mechanical properties of coal are significantly affected by temperature, and the mechanical strength of coal is negatively correlated with temperature [9,10]. Most studies on the temperature heterogeneity of coal mechanical strength are based on conditions such as low temperature and rapid heating [9,11–13], and few scholars have paid attention to the changes in the mechanical strength during CSC. Although experiments are the most direct way to study coal thermal damage, they are unable to effectively access the evolution of its micromechanical behavior, while the advantages of numerical simulation in data quantification and result visualization can well solve these problems. There are many commercial software programs (e.g., Abaqus, Comsol, Flac2D, and PFC2D) for studying thermal damage in rocks, and most of them are based on the continuous medium theory, while coal thermal damage is more consistent with the discrete medium theory. Based on the discrete medium assumption, PFC2D can simulate the thermodynamic behavior of a medium from a microscopic point of view, which can effectively study the rock thermal damage [14,15]. Most discrete media simulations concentrated on geotechnical and geological fields [16–19], with little attention paid to CSC.

In conclusion, thermal damage triggers a series of parameter changes in the physicochemical properties of coal, which has a great impact on its internal seepage capacity and is an important factor in the development of CSC. At present, many scholars have conducted a lot of studies on coal thermal damage, mainly focusing on the evolution of pore structure and changes in mechanical behavior induced by thermal damage. However, most studies are dominated by the result elaboration and lack further analysis. The characteristics of structural thermal damage induced by CSC have not been clarified, and the changes in micromechanical behavior during CSC are not yet clear. Based on this, through physical experiments, theoretical analyses and numerical calculations, this paper aims to investigate the thermal damage characteristics and micromechanical behaviors of structures induced by CSC. The results are of great practical significance for further revealing the development mechanism of CSC and for better prevention and control of CSC.

2. Experiments and methods

2.1. Sample preparation

Low-rank coals include lignite, gas coal, fertilizer coal, and long-flame coal. Lignite is widely distributed in northern China, and its pore structure is more developed and more sensitive to heat. Its physical and chemical properties are typical among the low-rank coals. For this reason, lignite was selected for this study. Coal samples were collected from the Shengli Coal Mine (SL) in Inner Mongolia Autonomous Region, China. The coal is lignite. Prior to the experiment, the coal samples were formed into $\varphi 25\text{ mm} \times 50\text{ mm}$ cores and selected for testing with high surface integrity. To ensure the similarity of the samples, all samples were prepared under the same experimental conditions ($T = 25^\circ\text{C}$, $P = 0.1\text{ MPa}$). The samples were divided into two groups for nuclear magnetic resonance (NMR) tests and mechanical experiments. The proximate analyses of coal samples are shown in Table 1.

2.2. Experimental procedure

The experimental process is sequentially high-temperature treatment, NMR test, scanning electron microscopy (SEM) test and uniaxial compression (UC) test, and the experimental procedure is shown in Fig. 1.

- (1) High-temperature treatment: CSC results from the physical and chemical reaction of many scattered coals over a long period of time [20]. Prior to heat treatment, the samples were placed in a crucible and completely coated with coal particles, as shown in Fig. 1, to simulate real CSC conditions. The boundary value for coal oxidation and combustion during CSC is typically 300°C , and the reaction is essentially over by 550°C [20–23]. For this, the heat treatment was programmed with six target temperatures (25°C , 100°C , 200°C , 300°C , 400°C , and 500°C), and the samples were kept at a constant temperature for 50 min at each target temperature to reach thermal equilibrium. After heating, the samples were placed in air for natural cooling. Experimental and parallel samples were heat-treated in the same environment and used for NMR test and SEM test, respectively.
- (2) NMR test: The samples were cooled and then subjected to negative pressure degassing in a vacuum water saturation device for 6 h. Subsequently, they were immersed in a constant pressure environment for 20 h to achieve full water saturation. The T_2 spectrum (S_w) and NMR image of saturated sample can be obtained by NMR test. Finally, the T_2 spectrum (S_{ir}) of dried sample was obtained by dehydrating the sample using a drying device and performing the NMR test again.

Table 1
Proximate analyses of coal samples.

Sample ID	Proximate analysis					Quality (g)
	M_{ad} (%)	A_d (%)	V_{ad} (%)	FC_{ad} (%)	$Q_{b,ad}$ (J/g)	
SL	15.27	3.24	32.82	49.16	22724.48	24.21

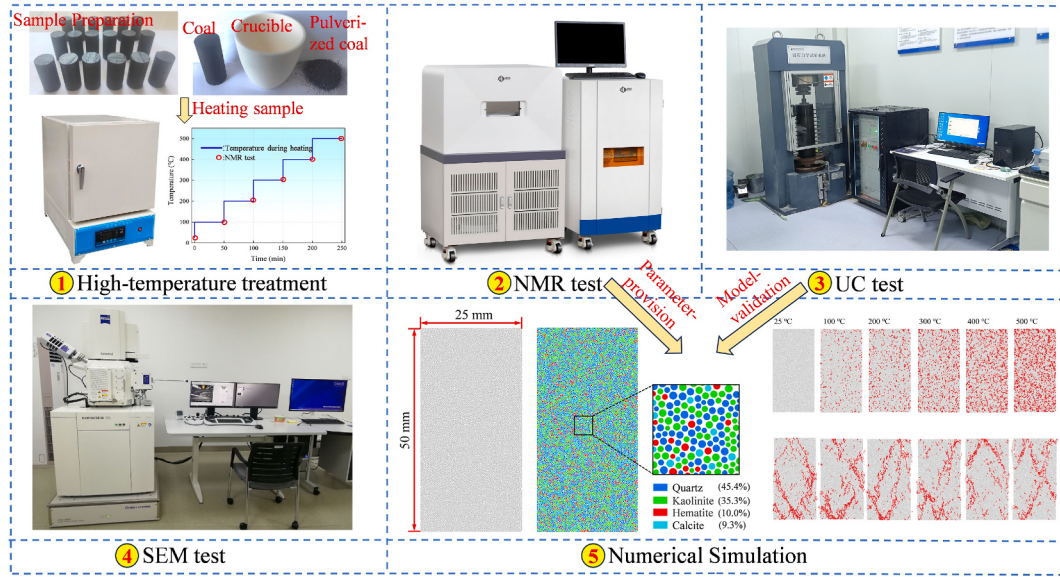


Fig. 1. Research process.

- (3) UC test: The heat-treated samples were subjected to a UC test using a servo press. The test was conducted by applying displacement loading at a rate of 0.2 mm/min until the sample was damaged.
- (4) SEM test: the samples were heat-treated and then hammered into blocks less than 10 mm in length. Trace blocks were taken for gold spraying and corresponding SEM images were obtained by SEM test.

2.3. Principles and theory of NMR

2.3.1. Principles of low-field NMR relaxation

Low-field NMR is a physical process that involves exciting hydrogen atoms (HA) using an external low magnetic field [24]. During this process, the HA align and interact with the external magnetic field. The Radio Frequency is withdrawn from the magnetic field after the HA have fully reached the excited state, and the relaxation time and distribution of the HA can be obtained by obtaining the signal during this decay process. T_2 relaxation is more accessible and is a common relaxation type to characterize coal pore structure [25]. Generally, it is subject to three relaxation mechanisms: free relaxation (T_{2B}), surface relaxation (T_{2S}) and diffusion relaxation (T_{2D}) [26]:

$$\frac{1}{T_2} = \frac{1}{T_{2B}} + \frac{1}{T_{2S}} + \frac{1}{T_{2D}} \quad (1)$$

In general, T_{2B} is much smaller than T_{2S} , so it can be ignored. Similarly, T_{2D} can be neglected when there is no magnetic field gradient or when the GT_E value is very small. Equation (1) can be simplified as:

$$\frac{1}{T_2} = \frac{1}{T_{2S}} = \rho_2 \left(\frac{S}{V} \right) \quad (2)$$

Where ρ_2 is the transverse surface relaxation rate, $\mu\text{m}/\text{ms}$; S is the surface area, cm^2 ; and V is the volume, cm^3 .

2.3.2. Principles of NMR imaging (NMRI)

NMRI performs spatial localization of signals by applying three mutually perpendicular and controllable gradient magnetic fields to the sample, with three orientation codes (level code, phase code, and frequency code) based on the differences in magnetic field strengths in different orientations on the sample [27,28]. These three codes are equivalent and interchangeable, and any two of them can be used to obtain some kind of localization, ultimately resulting in a NMRI of the sample in any section.

(1) NMRI direction

When performing an NMRI experiment, it is first necessary to determine the three imaging directions (level, phase, and frequency) of the sample, from which three sections are formed, namely, the sagittal plane, the transverse plane, and the coronal plane. As shown in Fig. 2, with X-axis as the level, Z-axis as the phase, and Y-axis as the frequency, then the sagittal plane imaging can be obtained; With X-axis as the frequency, Z-axis as the level, and Y-axis as the phase, then the coronal plane imaging is obtained; With X-axis as the

frequency, Z-axis as the phase, and Y-axis as the level, then the transverse plane imaging can be obtained.

(2) NMRI location and thickness

After determining the orientation of the NMRI, it is also necessary to obtain the position and thickness. The initial magnetic field is uniformly distributed and the field strength at any point A in the field is B_0 . After adding the gradient field (G_x, G_y, G_z), the field strength $B_{x,y,z}$ and frequency $f_{x,y,z}$ of point A are:

$$B_{x,y,z} = B_0 + G_x \cdot x + G_y \cdot y + G_z \cdot z \quad (3)$$

$$f_{x,y,z} = \gamma B_{x,y,z}$$

Where γ is the spin ratio, $\gamma = 42.58 \text{ MHZ/T}$. Therefore, the NMRI location can be determined through a gradient field. Any point in the magnetic field has an initial frequency, and the coordinates of the frequency codes can be obtained from the deviation degree of the center frequency. In this experiment, only the Z-axis was used as the level direction of the sample, from which the NMRI location was obtained.

The thickness of the plane depends on the soft pulse width and gradient strength, which are directly proportional to each other, and the expression for the thickness is given below:

$$h = \frac{2}{t_p G_s \gamma} \quad (4)$$

Where h is the plane thickness, cm; t_p is the pulse width, cm; G_s is the gradient strength, Gs/cm.

2.3.3. Permeability

The NMR permeability can be obtained from the pore parameters, and the free fluid intensity (FFI) and bound fluid intensity (BFI) are the key to solving the permeability, which is shown in Fig. 8. The cumulative porosity corresponding to the T_2 spectrum of saturated samples is the TFI porosity, and the cumulative porosity corresponding to the T_2 spectrum of dry samples is the BFI porosity, and the difference between the two is the FFI porosity. In this paper, coal permeability is obtained from a modified Coates model [2] :

$$k = \left(\frac{\phi}{A} \right)^{a1} \left(\frac{FFI}{BFI} \right)^{b1} \quad (5)$$

Where k is the permeability, mD; ϕ is the porosity, %; A , $a1$ and $b1$ are coefficients related to coal properties: $A = 0.0109$, $a1 = -0.44$, $b1 = 1.33$.

2.4. Numerical simulation

The PFC2D numerical model is based on discrete rigid particles, which are independent and freely moving particles that generate forces or moments by contacting each other. Different particle sizes and particle contact patterns affect the mechanical strength of the sample [14,29]. Parallel viscous models are suitable for modelling the movement of particles with different mineral compositions, and

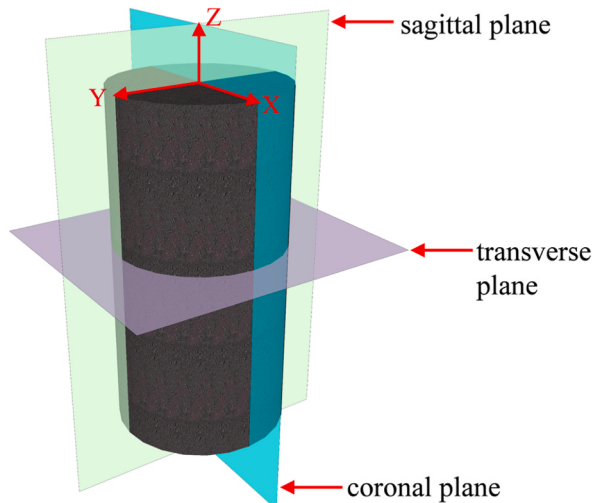


Fig. 2. Imaging orientations of sagittal plane, transverse and coronal plane of the sample.

thus serve as a model for particle contact.

The PFC2D numerical model can be used to study the thermal strain due to temperature. In this model, thermal strain is achieved by controlling the particle size and the force carried by each parallel bond [14] :

$$\Delta R = \alpha R \Delta T \quad (6)$$

Assuming that particle expansion produces only normal stress increments ($\Delta \bar{F}^n$) and that the contact radius(\bar{L}) expands uniformly, there is:

$$\Delta \bar{F}^n = -\bar{K}^n A \Delta U^n = -\bar{K}^n A (\bar{\alpha} \bar{L} \Delta T) \quad (7)$$

Where Δ denotes the variation, dimensionless; α is the thermal expansion coefficient, $1/K$; R is the particle radius, m ; T is the temperature increment, K ; \bar{K}^n is the normal stiffness, N/m ; A is the contact area, m^2 ;

2.4.1. Basic parameters

The macroscopic mechanical parameters obtained through experiments are not directly used for discrete element simulations, and matching microscopic parameters need to be obtained as well [30]. The main methods for calibrating microscopic parameters are trial-and-error method, orthogonal test and iterative algorithm [31–33]. The trial-and-error method is recognized as a more accurate method to calibrate the microscopic parameters, but due to the shortcomings of time-consuming and heavy workload, some scholars have proposed the orthogonal test and iterative algorithms to improve the efficiency of the microscopic parameter calibration. To ensure the accuracy of the microscopic parameters, the trial-and-error method was used to calibrate the microscopic parameters, as shown in Table 2.

2.4.2. Model construction

The numerical model is a rectangular geometric model with a length of 50 mm and a width of 25 mm, and the porosity is set to 12 %, which is consistent with the experimental parameters. The average radius of the particles was approximately 0.39 mm and a total of 9017 particles were generated, as shown in Fig. 3. The thermodynamic behavior of coal is more significantly affected by its mineral content and composition [10,34], thus the numerical models for different mineral components were considered. In conjunction with the experimental results [35,36], the sample was set to consist of four minerals, and the linear expansion coefficient α and specific heat capacity C_p were assigned to each mineral, as shown in Table 3.

2.4.3. Simulation procedure

Based on the model, the samples were heated and loaded. To reduce thermal stress errors caused by differences in linear expansion coefficients, it is assumed that the temperature of samples varies uniformly, with a heating range of 25–500 °C and a temperature increment of 2 °C. When the heating was complete, the sample was cooled. The top and bottom of the samples were set as loading boundaries and UC tests were simulated by exerting boundary displacements, and the loading rate was set at 0.05 m/s.

3. Results and discussion

3.1. Characterization of structural damage induced by CSC

3.1.1. Macrostructural damage characterization

During CSC, temperature changes the physical and chemical properties of coal, thus affecting its macroscopic form [37]. The process of CSC can be divided into dry degassing stage and coal pyrolysis stage. In the dry degassing stage ($T = 25$ –200 °C), the increase in temperature leads to intensified water evaporation and gas desorption of coal, accompanied by a decrease in matrix quality [23]. During the pyrolysis stage, which takes place between 200 and 500 °C, the coal undergoes further decomposition, resulting in the production of significant amounts of volatile substances such as gases and tars, which further degrade the quality of the coal [9]. As a result, cracks appeared on the surface of the SL sample at 100 °C. These cracks increased significantly with rising temperature, and the coal body deformed accordingly (see Fig. 4). Dehydration of the coal matrix and escape of CH₄ molecules are the main reasons of coal deformation [38,39].

The MRI equipment acquires the spatial position of hydrogen protons by two codes, which form a data matrix and are converted into an MRI image of the sample [40]. In the NMR image, the colors corresponding to the hydrogen proton signals from high to low are

Table 2
Mechanical micro-parameters of the sample model.

Micro-parameter	Value	Micro-parameter	Value
Maximum particle radius, R_0 (mm)	0.49	Parallel bond radius multiplier	1.00
Minimum particle radius, R_l (mm)	0.30	Parallel bond effective modulus, \bar{E}_c (GPa)	0.60
Effective modulus of model , E_m (GPa)	0.60	Ratio of normal stiffness to shear stiffness of parallel bond, \bar{k}_n/\bar{k}_s	2.50
Effective modulus of particles , E_c (GPa)	0.60	Mean tensile strength of parallel bond, σ_t (MPa)	10.00
Ratio of normal stiffness to shear stiffness of particle , k_n/k_s	2.50	Mean shear strength of parallel bond, σ_c (MPa)	5.00
Friction coefficient of particles, μ	0.58	Parallel bond friction angle, φ	45.0

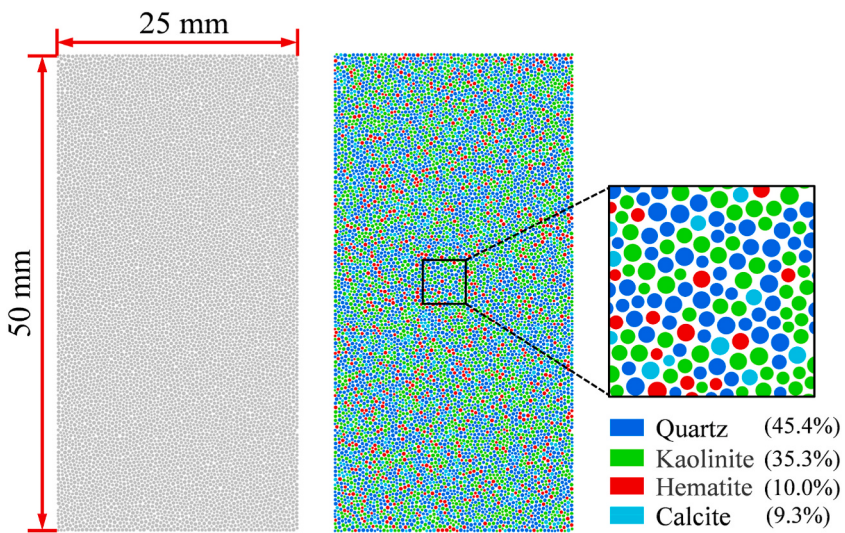


Fig. 3. Numerical model for different mineral compositions.

Table 3
Model parameters for different mineral components.

Mineral Name/Percentage	α (K^{-1})	C_P (J/(kg·K))
Quartz (45.4 %)	2.4e-5	730
Kaolinite (35.3 %)	7.27e-6	600
Hematite (10.0 %)	6.00e-6	670
Calcite (9.3 %)	1.31e-5	473

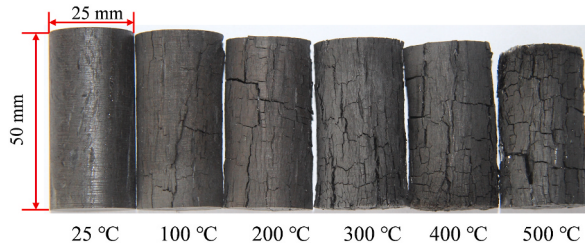
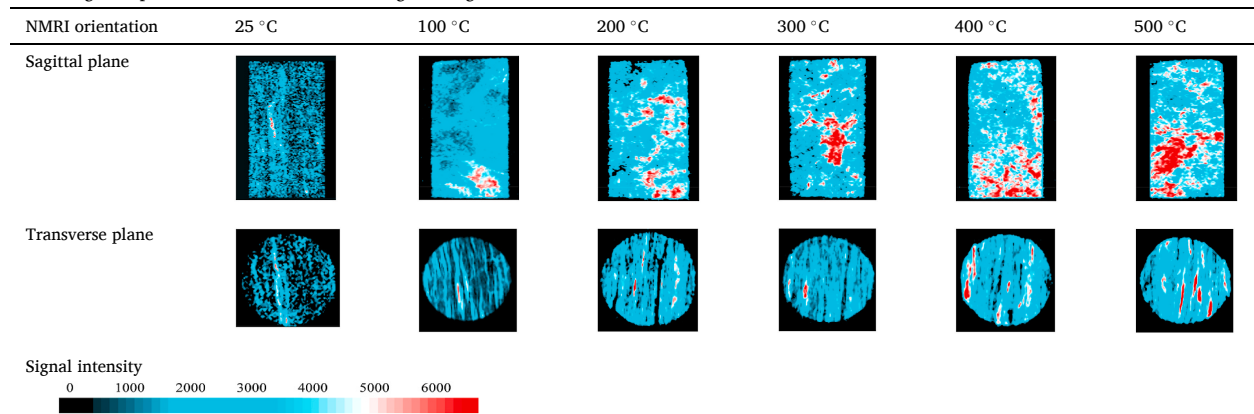


Fig. 4. Macroscopic morphology of SL sample at different temperatures.

Table 4
NMI images of pore structure evolution during heating.



red, green, and blue (Table 4), respectively, with higher hydrogen proton signals representing better pore development. In the initial state (25°C), the colors of the hydrogen proton signals of the sample were mainly blue and light green, indicating an underdeveloped pore structure. The green proton clusters of the sample increase with increasing temperature, indicating the developed pore structure. At 300°C , the red proton clusters start to increase and there are obvious cracks inside the sample. After the temperature exceeded 300°C , the number of red plasmonic clusters increased significantly, and the pores and cracks expanded and connected rapidly, eventually forming short and numerous complex pore structures in the sample.

3.1.2. Microstructural damage characterization

The microstructure evolution of SL sample with temperature is shown in Fig. 5, and the magnification of all these images is 1500 times. Overall, the microstructures of the sample at different temperatures exhibit different microscopic features. In the original state, the surface of the coal is relatively smooth, and there are only a few microfractures (see Fig. 5a). These microfractures were formed during the coal's creation and are not related to each other. As the temperature increases, the coal surface begins to become roughened, the number of pores increases and is independently distributed, and pores are also created between the clusters of mineral particles and the organic matter (Fig. 5b and c). When the temperature reaches 300°C , the coal surface becomes rougher, and the cracks expand and connect with each other to form differently shaped pore structures (Fig. 5d). With further increase in temperature, the coal has undergone thermal deformation, some minor and medium pores are connected into large pores, and irregular pores are distributed on the coal surface to form a more complex pore structure (Fig. 5e and f).

3.2. Characterization of pore parameter evolution during CSC

3.2.1. NMR T_2 distribution

The NMR normalized signal is the ratio of the relaxation signal to the sample mass [8]. Coal typically exhibits a T_2 relaxation time between 0.1 and 10000 ms, with longer relaxation times corresponding to larger pore spaces [41]. Generally, the T_2 distribution of a coal will show three peaks (P1, P2, and P3), which correspond to the microporous (<10 ms), the mesoporous (10–100 ms), and the macroporous (>100 ms).

As shown in Fig. 6a, under the initial state (25°C), the saturated sample is mainly dominated by the P1 peak, indicating that the initial pore structure is mainly dominated by micropores. From 25°C to 300°C , the P1 peak decreased significantly, while the P2 peak increased and the P3 peak was slightly elevated. This indicates that the micropores underwent a transition to mesopores, with a small number of macropores also forming. As the temperature increased ($300\text{--}400^{\circ}\text{C}$), more meso- and macropores were produced and the P2 peak was substantially increased. At 500°C , the P1 peak disappeared and the P3 peak significantly increased, suggesting that the micropores had fully transformed into meso- and macropores. It can be seen that the pore development of low-rank coal during CSC is evident.

The T_2 relaxation time of dried sample was essentially less than 100 ms (Fig. 6b). Overall, the dried sample contained only one peak (P1), indicating that the trace moisture in the dried coal was concentrated in the micropores. The residual moisture of the dried sample decreases as the temperature increases. This is because the moisture in the highly permeable meso- and macropores evaporates completely during drying, while the moisture in the low-permeability micropores does not.

3.2.2. Distribution of pore throat, porosity and permeability

The channel that connects the pores within the coal is known as the pore throat. The permeability between the pores increases with the increase in the pore throat [25]. The pore throat distribution of SL sample is shown in Fig. 7a, and the pore throat ratio changes significantly with increasing temperature. Form $25\text{--}100^{\circ}\text{C}$, the proportion of microporous ($r < 0.1 \mu\text{m}$) pore throats decreased sharply, and the proportion of meso- and macroporous ($r > 0.1 \mu\text{m}$) pore throats gradually increased. From 100 to 500°C , the proportion of microporous pore throats gradually decreased or disappeared, and the proportion of meso- and macroporous pore throats continued to increase. To provide a more intuitive characterization of the pore variations, we introduce the equivalent average radius of the pores

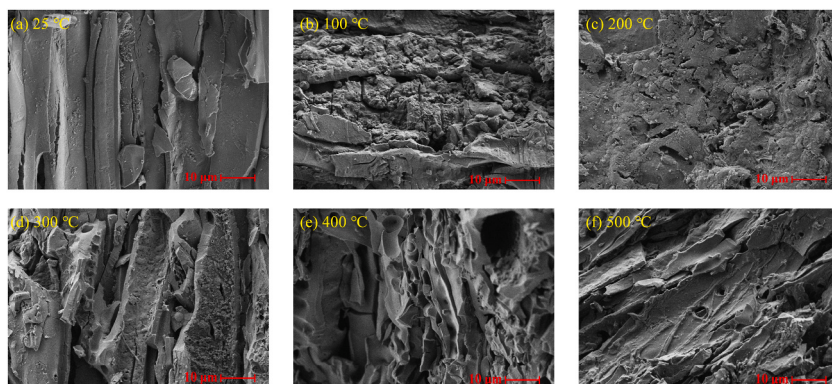


Fig. 5. SEM images of SL sample at different temperatures.

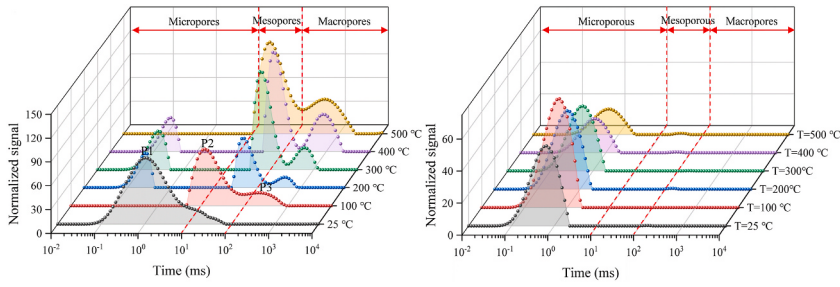


Fig. 6. Distribution of T_2 spectrum with temperature. (a) saturated sample; (b) dried sample.

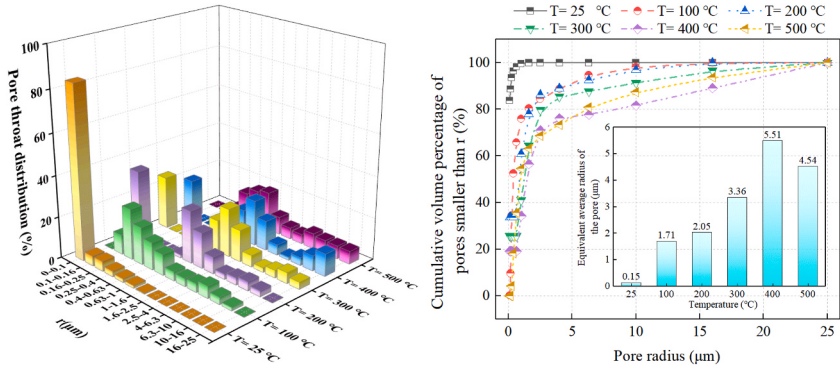


Fig. 7. Evolution of pore throat and pore radius with temperature. (a) pore throat distribution; (b) equivalent average radius.

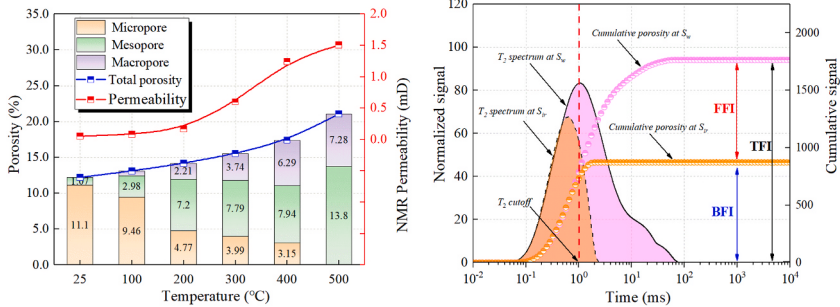


Fig. 8. Porosity, permeability and $T_{2\text{cutoff}}$. (a) porosity and permeability; (b) Solution for $T_{2\text{cutoff}}$.

[42]: $r_m = \sum \omega_i r_i / \sum \omega_i$; where r_i is the pore radius, μm ; ω_i is the cumulative porosity when the pore radius is r_m . As shown in Fig. 7b, the initial r_m of SL sample is low ($0.15 \mu\text{m}$), and the r_m increases with increasing temperature up to $5.51 \mu\text{m}$. It is evident that severe thermal damage already occurs in low-rank coals at temperatures below 100°C , and their pore structure develops further in the high temperature stage.

Porosity can be determined by converting the water signal per unit volume of the sample [25]. Different types of porosity can be obtained based on the relaxation time, as illustrated in Fig. 8. Overall, the porosity and permeability of the SL sample have a tendency to increase with temperature. The initial porosity and permeability were 12.21 % and 0.05 mD, respectively; with the increase in temperature, the porosity reached up to 21.05 %, which was 72.42 % higher than the initial porosity. The change in permeability was not significant before 300°C , but sharply increases after 300°C , reaching a maximum of 1.51 mD.

3.3. Macro- and micromechanical behavior

Under experimental conditions, the initial stress peak of SL sample was 9.08 MPa, and the stress peak suddenly dropped to 1.89 MPa at a temperature of 100°C , which indicated that the coal sample underwent a significant physical change at 100°C . The stress exhibited a consistent fluctuation as the temperature increased (Fig. 9a). The peak strain of the SL sample remained low until 200°C , after which it increased due to the development of the coal pore structure at high temperatures, which prolonged the compacting

process [10]. It can be seen that the numerical results are similar to the experimental results (Fig. 9b and c), which is a critical validation of the numerical model. Experimental results show that the evolution of pores and fissures during CSC affects its thermodynamic behavior. According to Fick's law and the fracture mechanics theoretical model, the generation and expansion of pores and fissures caused by thermal stress will reduce the mechanical strength of the coal and increase the contact area between the coal matrix and oxygen, which promotes the diffusion of internal oxygen and accelerates oxidative reactions. According to Fourier's law of heat conduction, the oxidation reaction leads to a decrease in the thermal conductivity of coal matrix, allowing heat to build up locally and further promoting coal combustion.

As is well known, thermal stress can cause cracking and fracturing of coal bodies [43–45]. Fig. 10a shows the evolution of thermal cracks with temperature for SL sample, with gray representing the coal body and red representing the cracks. From 25 °C to 100 °C, a small amount of microcracks are distributed in the sample, which are mainly concentrated on the side walls. From 100 °C to 300 °C, microcracks spread from the wall edges to the centre, with an associated increase in number. When the temperature exceeds 300 °C, more cracks are observed in the samples, some of which are clustered into clusters. Fig. 10b illustrates that the damage pattern of the sample changes with temperature. At 25 °C, the samples experienced oblique shear damage, and the cracks were concentrated on the lower side. From 100 °C to 200 °C, the cracks in the samples began to concentrate on the upper surface as the temperature increased. From 300 °C to 400 °C, several sets of microcracks were produced in the samples and the damage was mainly in the form of crack networks. At 500 °C, an X-shaped diagonal shear damage pattern of primary cracks and secondary fractures. It is worth noting that coal damage patterns during loading are influenced by heat cracking caused by high temperatures.

Fig. 11 illustrates the crack development in the heat-treated sample during numerical loading. At 25 °C and loaded to point a ($\epsilon = 0.798 \times 10^{-2}$, $\sigma = 5.536 \text{ MPa}$), shear cracks begin to appear in the sample. When the sample was loaded to point b ($\epsilon = 0.963 \times 10^{-2}$, $\sigma = 6.714 \text{ MPa}$), the shear cracks increased and tensile cracks began to appear. Subsequently, before reaching the peak point c ($\epsilon = 1.283 \times 10^{-2}$, $\sigma = 8.613 \text{ MPa}$), both shear and tensile cracks increase with the loading process, with shear cracks increasing much faster than tensile cracks. After reaching the peak c point, the shear and tensile cracks in the samples increased dramatically, and the growth rates of the two types of cracks are similar. In contrast, the cracks produced in the heat-treated samples during loading were mainly tensile cracks, while shear cracks accounted for only a small proportion. From 100 °C to 500 °C, the micromechanical behavior of the samples is similar, with a small variation of the critical value with temperature.

3.4. Sensitivity analysis of micromechanical behavior

3.4.1. Effect of particle size on micromechanical behavior

Coal consists of different mineral particles, and the particle size has a direct influence on its thermal effect, which in turn affects its micromechanical behavior [46]. From a microscopic perspective, the particle sizes between the minerals within the coal are different, ultimately leading to different forms of heat induction [47]. Therefore, it is of practical significance to study the effect of particle size on coal thermal damage. The minimum particle size of the particles in the numerical model was set to 0.3, 0.4, 0.5 and 0.6 mm, which resulted in 9317, 5067, 3253 and 2262 particles, respectively. Based on the simulation conditions in Section 3.3, the effect of particle size on the micromechanical behavior was investigated by varying the minimum particle size (mps) of the particles.

The variation of thermal cracks with temperature for samples with different particle sizes is shown in Fig. 12. When the mps is 0.3 mm, the sample generates the most particles, and the contact between particles during the heating is the highest, forming a high-density crack distribution. When the mps is 0.4 mm, the number of particles generated in the sample decreases, and the contact between particles during heating is higher, and there is still a higher density of crack distribution. When the mps is 0.6 mm, the sample

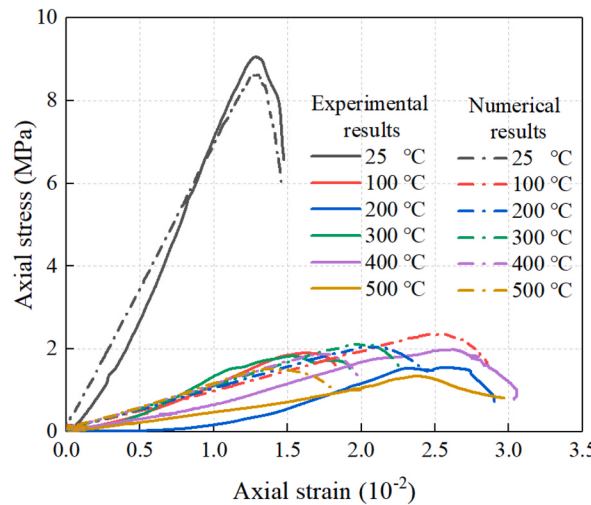


Fig. 9. Experimental and numerical results of uniaxial compression experiments of SL sample at different temperatures.

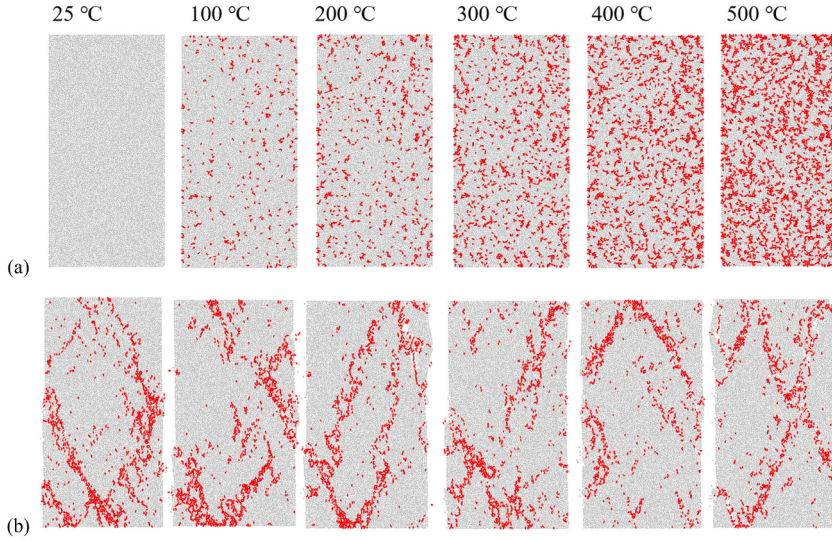


Fig. 10. Crack distribution of SL sample during heating and loading. (a) thermal cracks; (b) compression cracks.

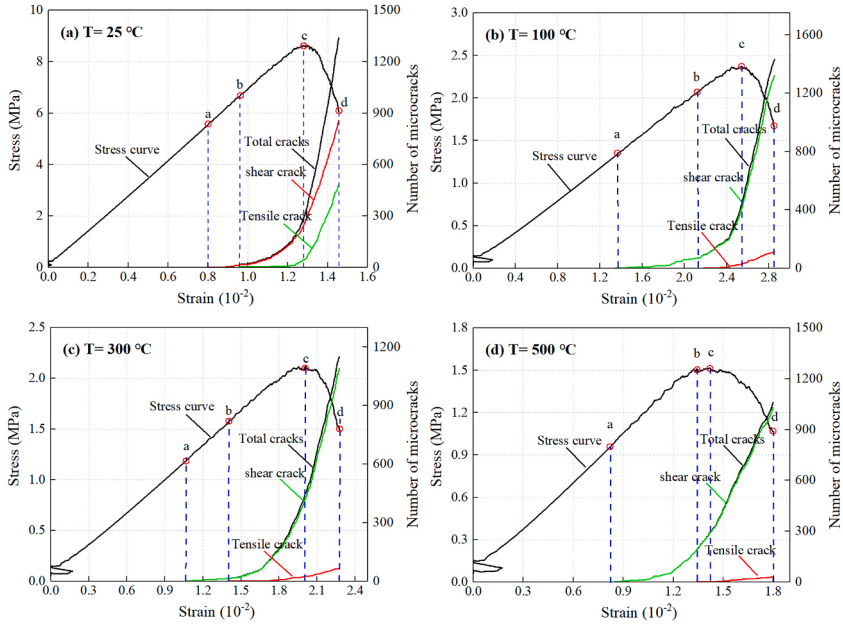


Fig. 11. Crack development during sample loading at different temperatures.

generates the least number of particles, and the contact between the particles during the heating is minimized, forming a low-density crack distribution.

Fig. 13 demonstrates the relationship between thermal cracks and peak stresses of coal samples with temperature for different particle sizes, and they all show a good exponential relationship ($R^2 > 0.98$). At 100 °C, the number of thermal cracks generated in the 0.3–0.6 mm particle interval were 484, 215, 150 and 123, respectively. With further increase in temperature, their values were elevated to 3310, 1819, 1280 and 826 at 500 °C, respectively. At 100 °C, the peak stresses generated in the 0.3–0.6 mm particle interval were 8.63, 8.65, 8.53, and 7.88, and their values decreased to 1.52, 1.57, 1.47, and 1.62 at 500 °C, respectively. It can be seen that the increase in particle size promotes thermal cracking in general, and at the same temperature, thermal cracks increase with decreasing particle size. The variation in particle size has a small effect on the peak stress of the samples.

To better illustrate the robustness and reliability of the simulations, sensitivity analysis of the simulation parameters at different particle sizes were performed. Different particle size intervals were set up to compare the cracks number and the variation rate of peak stress with temperature for different intervals, as shown in Table 5. As the particle size interval increases, the average variation rate of crack number with temperature decreases from 41.41 % to 24.98 %. In the interval of 0.4–0.6 mm, the average variation rate is close

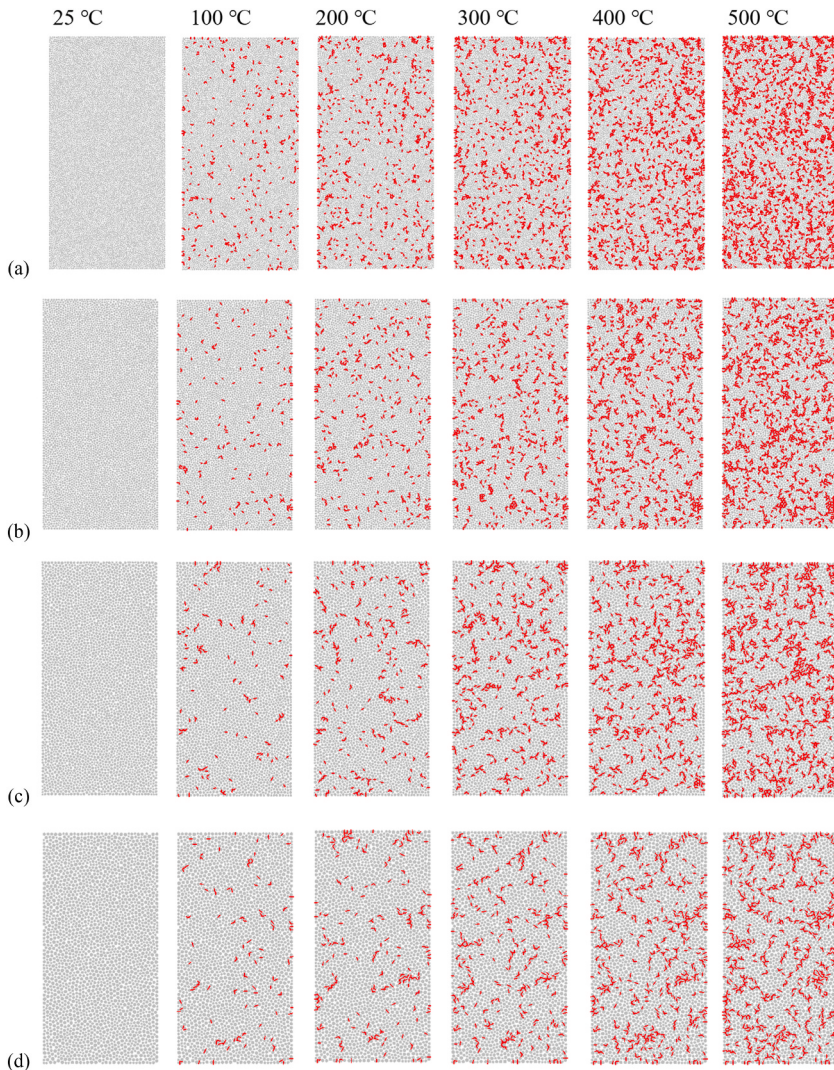


Fig. 12. The variation of thermal cracks with temperature for samples with different particle sizes. (a) mps = 0.3 mm; (b) mps = 0.4 mm; (c) mps = 0.5 mm; (d) mps = 0.6 mm.

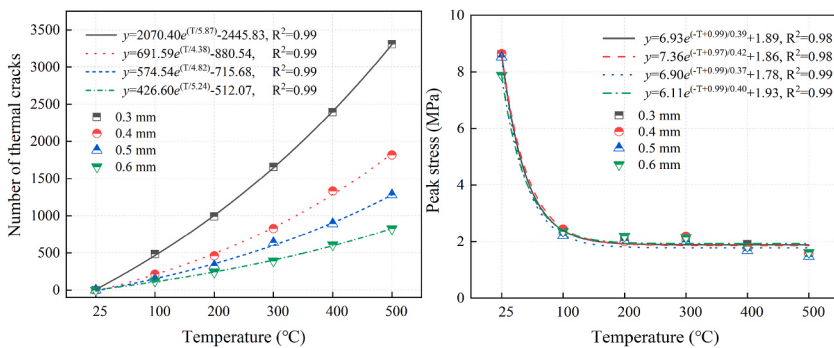


Fig. 13. The variation of the number of thermal cracks and peak stress with temperature for samples with different particles. (a) thermal cracks; (b) peak stress.

Table 5

Sensitivity analysis of simulation parameters at different particle sizes.

Temperature (°C)	Variation rate of the number of cracks (%)			Variation rate of peak stress (%)		
	[0.3,0.4]	[0.4,0.5]	[0.5,0.6]	[0.3,0.4]	[0.4,0.5]	[0.5,0.6]
25	0.00	0.00	0.00	0.23	-1.41	-7.54
100	-55.58	-30.23	-18.00	3.28	-9.81	7.09
200	-53.54	-28.91	-25.69	-3.67	1.84	8.07
300	-49.97	-23.04	-38.87	3.89	-9.49	8.33
400	-44.32	-32.93	-31.88	-8.17	-4.20	8.64
500	-45.05	-29.63	-35.47	3.65	-6.19	9.74
Average value	-41.41	-24.13	-24.98	-0.13	-4.88	5.72

Note: [0.3,0.4] represents the interval of particle size between 0.3 and 0.4, mm.

within. The average variation rate of peak stress increases with particle size from 0.13 % to 5.72 %, and they are not simple linear trends. Overall, the variation of particle size parameters had a significant effect on the simulation results. the smaller particle sizes have a greater effect on the cracks number, and larger particle sizes result in more pronounced variations in the peak stress.

3.4.2. Effect of mineral components on micromechanical behavior

Coal is generally composed of a variety of minerals, and different mineral components have different thermal parameters, which have an effect on the development of thermal cracks [48,49]. In addition, different coals have different proportions of minerals and will exhibit different forms of thermal damage. Therefore, it is necessary to study the effect of mineral components on coal thermal damage. Based on the simulation conditions in Section 3.3, the proportions of coal mineral composition was set to four plans, as shown in Table 6.

The variation of thermal cracks with temperature for coals with different mineral components proportions is shown in Fig. 14. In plan 1, the contact of thermal expansion between particles during heating is the highest, forming a high-density crack distribution. For plans 2, 3 and 4, there is less contact of thermal expansion between particles during heating, forming a low-density cracks distribution. Overall, the development of thermal cracks of quartz-dominated coal is strongly influenced by temperature, while the cracks development of coals with proportions of other mineral fractions is less affected by temperature.

Fig. 15 demonstrates the relationship between thermal cracks and peak stresses with temperature for coal samples with different mineral proportions, and they all show a good exponential relationship ($R^2 > 0.99$). Overall, the number of thermal cracks in coal increases linearly with temperature in all plans. For plans 2, 3 and 4, the increase in the number of thermal cracks is significantly smaller than for plan 1, which is due to the differences in thermal parameters between the minerals. In contrast, quartz has a higher value of the thermal parameter, and the remaining three minerals have relatively low and close values of the thermal parameter, so that there is an increase in the thermal expansion between the particles when quartz is the dominant, and a similar form of thermal expansion in the coal samples of the remaining three mineral proportions. However, the peak stress of coal varies relatively little with the mineral composition. Therefore, the mineral components can affect the density of thermal crack distribution, but the effect on the mechanical strength is small.

Sensitivity analysis of the simulated parameters for different mineral composition proportions was performed to compare the ratios of the simulated parameters for different plans to plan 1, as shown in Table 7. The closer the ratio is to 1, the closer it is to the results of plan 1. The average ratio of the cracks number for the different composition plans to that of plan 1 ranged from 0.34 to 0.36, indicating that changing the ratio of mineral compositions leads to an overall decrease in the cracks number of about 65 %. The average ratio of different peaks stress ranged from 1.11 to 1.13. Overall, changing the ratio of mineral compositions had a significant effect on the cracks number and a small effect on the peak stress.

3.4.3. Effect of loading rate on micromechanical behavior

It was shown that the uniaxial compressive strength of coal increases with increasing loading rate [50–52]. However, most of the studies are based on experimental means to investigate the effect of loading rate on the mechanical strength of coal at room temperature, and few of them involve temperature-related studies. Therefore, it is necessary to investigate the effect of loading rate on thermal damage. The loading rates were set to 0.05, 0.1, 0.2 and 0.3 m/s based on the simulation conditions in section 3.3. Since the loading rate only has an effect on the mechanical properties of coal, this section will focus only on the mechanical properties of heat-treated coal after UC tests.

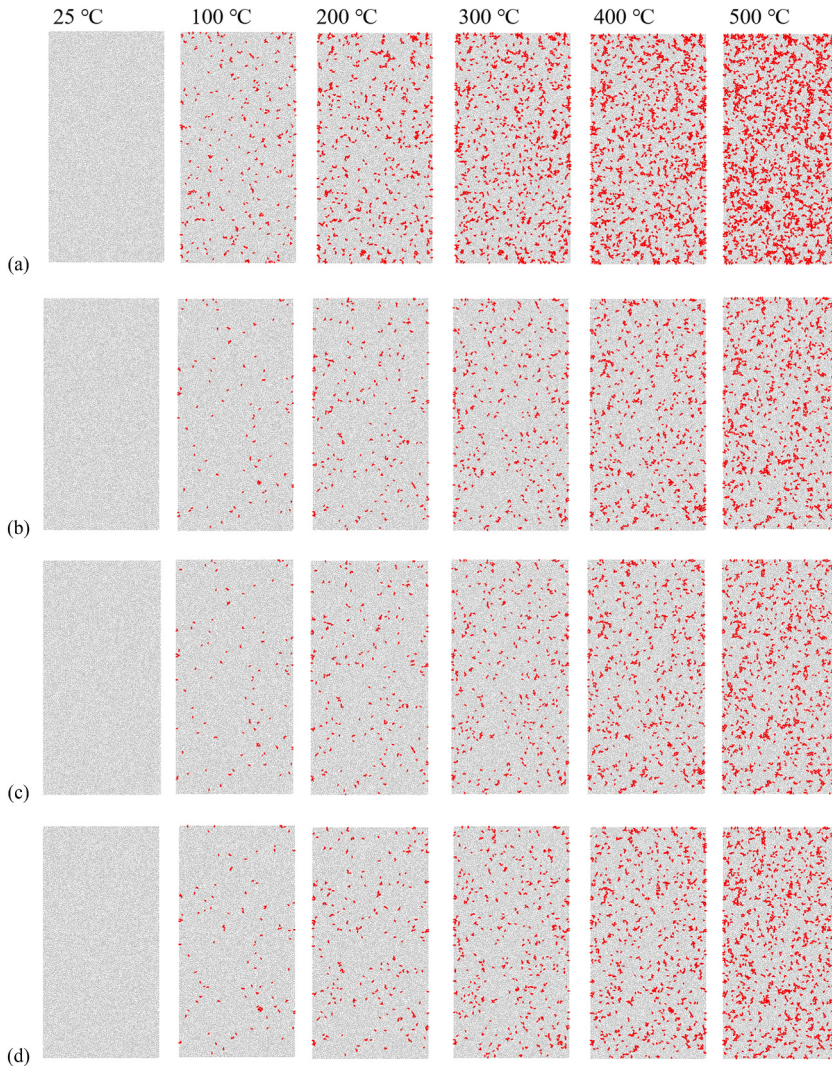
The variation of loading cracks with temperature for coal at different loading rates is shown in Fig. 16. Overall, the loading cracks of coal increased with the increase of loading rate, and some cracks connected with each other to form large cracks, which were mainly dominated by oblique shear damage. On the one hand, the increase of loading rate promotes the stress concentration, stress dynamic response and energy release of coal samples; on the other hand, the coupling of loading rate and temperature further promotes the transformation of stress distribution and capacity dissipation of coal samples.

Cracks develop slowly at lower loading rates, the stress distribution is more stable, and the stress concentration within the coal is not significant. As the loading rate increases, the crack development accelerates, and the stress distribution shows heterogeneity and stress concentration increases. The high temperature promotes the generation of thermal stresses within the coal, and the increased loading rate intensifies the inhomogeneous distribution of stresses under the effect of thermal stresses, contributing to the rapid

Table 6

Setting plan for the proportions of coal mineral components.

Mineral components	Plan 1	Plan 2	Plan 3	Plan 4
Quartz	40 %	20 %	20 %	20 %
Kaolin	20 %	40 %	20 %	20 %
Hematite	20 %	20 %	40 %	20 %
Calcite	20 %	20 %	20 %	40 %

**Fig. 14.** The variation of thermal cracks with temperature for coals with different mineral components proportions. (a) plan1; (b) plan2; (c) plan3; (d) plan4.

expansion and increase of cracks within the coal. This process accelerated the transition of crack development from microscopic to macroscopic and significantly increased the overall thermal damage degree of the coal body. It can be seen that the increase of temperature and loading rate will intensify the structural damage, stress concentration and crack extension of coal body, and their coupled effects together promote the thermal damage of coal.

Fig. 17 shows the variation of the number of UC cracks number and the peak stress with temperature for coal at different loading rates. Overall, the crack number in the heat-treated coal showed an increase and then a decrease with the loading rate (Fig. 17a), and the higher the loading rate, the higher the overall number of cracks. It is worth noting that the peak value of the number of compression cracks of heat-treated coal samples at different loading rates appeared at 100 °C, indicating that the coal samples underwent a significant physical change at 100 °C, which led to a drastic decrease in their load-bearing capacity, and thus it was easier to reach the

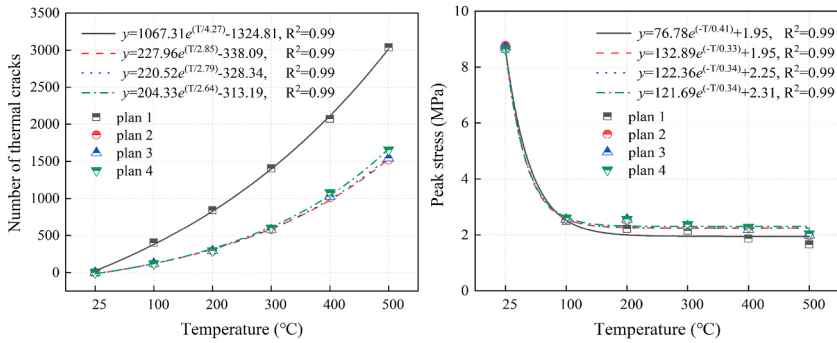


Fig. 15. The variation of the number of thermal cracks and peak stress with temperature for coals with different mineral components proportions. (a) thermal cracks; (b) peak stress.

Table 7

Sensitivity analysis of simulation parameters under different plans.

Temperature (°C)	Ratio of the number of cracks			Ratio of peak stress		
	N21	N31	N41	N21	N31	N41
25	—	—	—	1.01	1.01	1.00
100	0.30	0.30	0.30	1.02	1.03	1.05
200	0.34	0.35	0.35	1.14	1.15	1.16
300	0.41	0.41	0.43	1.09	1.08	1.10
400	0.49	0.50	0.52	1.19	1.17	1.22
500	0.50	0.51	0.54	1.19	1.20	1.23
Average value	0.34	0.34	0.36	1.11	1.11	1.13

Note: N21 represents the ratio of plan 2 to plan 1.

damage condition and produce more cracks. And then the number of cracks fluctuated with the increase of temperature, which is consistent with the experimental results. The peak stresses at different loading rates showed a favorable exponential relationship with temperature ($R^2 > 0.99$), and the peak stresses increased significantly with the increase in loading rate. This is because the increase of loading rate shortens the time for the coal body to fracture, limits the development of the pore-fracture system and reduces the mechanical damage, which improves the ability of the coal body to resist external deformation, and thus increases the compressive strength of the coal.

Sensitivity analysis of simulation parameters at different loading rates. Different loading rate intervals were set to compare the cracks number and the variation rate of peak stress with temperature for different intervals, as shown in Table 8. As the loading rate interval increases, the average variation rate of the cracks number with temperature decreases from 58.76 % to 23.44 %. The average variation rate of peak stress increased from 5.20 % to 10.94 %. Overall, the variation in loading rate has a very significant effect on the simulation results. Higher loading rates predict a higher overall number of cracks and a more significant increase in the variation rate of peak stress.

4. Conclusion

In this study, the thermal damage characteristics and micromechanical behavior of structures induced by spontaneous combustion of low-rank coal are investigated through physical experiments, theoretical analysis and numerical calculations. Experiments such as nuclear magnetic resonance, scanning electron microscopy and uniaxial compression were used to visualize and quantify the evolution of pore structure and structural strength during CSC. A multicomponent particle flow model of coal thermal fracture was developed to study the natural micromechanical behavior of coal and a sensitivity analysis was performed. The main conclusions are as follows.

- (1) During the CSC of low-rank coal, the micropores in coal gradually evolved into medium or large pores, and when the temperature exceeded 200 °C, the pore size of coal increased dramatically, up to 5.51 μm. The porosity and permeability of the coal both increase with increasing temperature, and their values can reach 21.05 % and 1.51 mD, respectively, indicating that thermal damage leads to a more loose and porous internal structure of the low-rank coal.
- (2) The mechanical strength of low-rank coal decreases sharply at 100 °C, resulting in a sharp decrease in its bearing capacity, which is more likely to reach the damage state and produce more cracks. Then, the thermal damage fluctuated with increasing temperature, indicating that the low-rank coals had experienced severe thermal damage at the early stage of CSC.
- (3) After heat treatment, the cracks type produced in low-rank coal during loading were mainly tensile cracks, while shear cracks accounted for only a small proportion. From 100 °C to 500 °C, the micromechanical behavior of low-rank coal is similar, and the

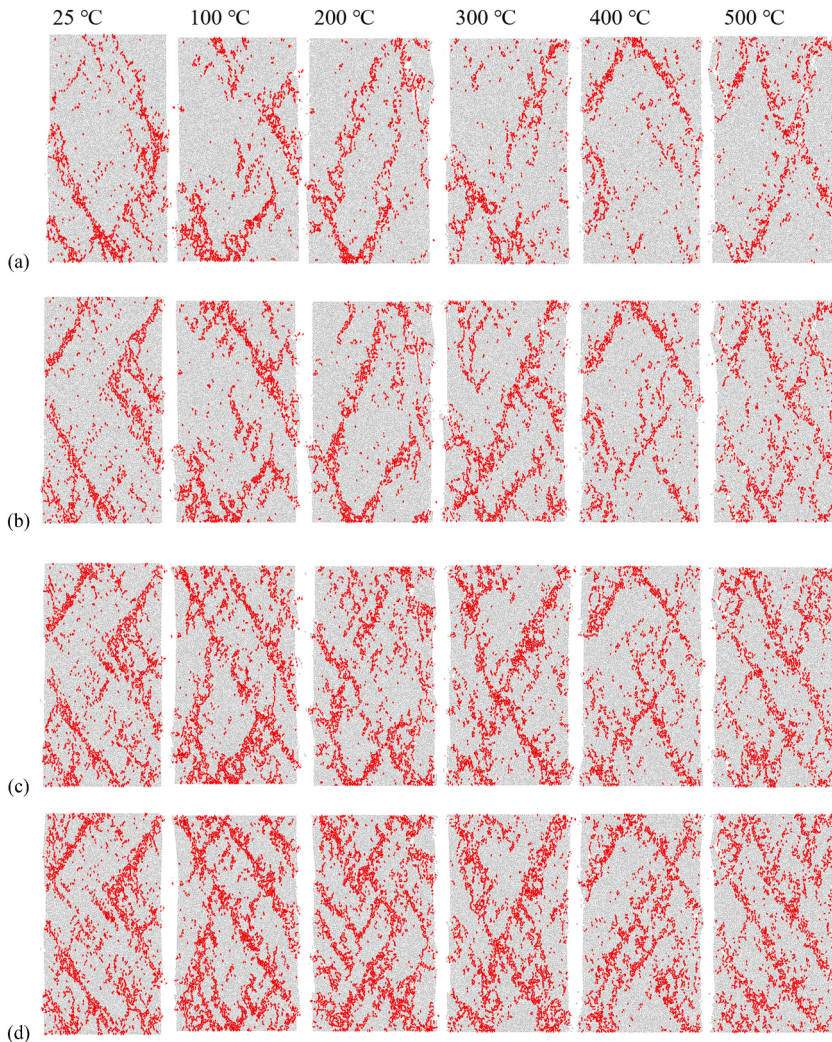


Fig. 16. The variation of loading cracks with temperature for coal at different loading rates. (a) loading rate = 0.05 m/s; (b) loading rate = 0.1 m/s; (c) loading rate = 0.2 m/s; (d) loading rate = 0.4 m/s.

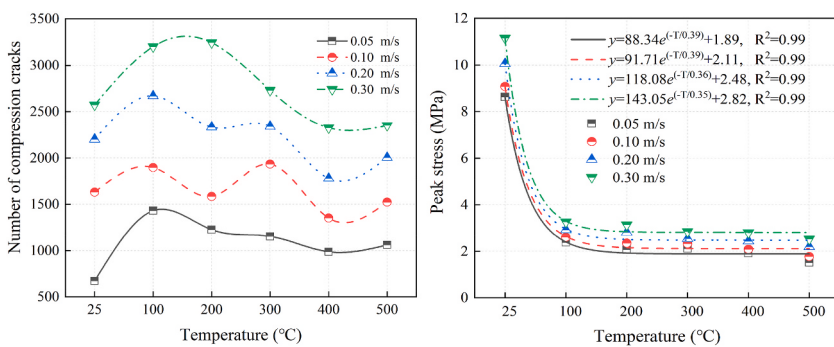


Fig. 17. The variation of the number of UC cracks and the peak stress with temperature for coal at different loading rates. (a) compression cracks; (b) peak stress.

Table 8

Sensitivity analysis of simulation parameters at different loading rates.

Temperature (°C)	Variation rate of the number of cracks (%)			Variation rate of peak stress (%)		
	[0.05,0.1]	[0.1,0.2]	[0.2,0.3]	[0.05,0.1]	[0.1,0.2]	[0.2,0.3]
25	142.35	34.95	16.90	5.20	10.81	10.94
100	32.63	40.62	19.97	9.87	12.03	11.75
200	29.26	47.10	39.09	13.52	19.59	11.84
300	67.68	20.93	16.67	9.66	9.42	12.32
400	36.98	31.58	30.75	9.09	16.75	15.15
500	43.64	31.56	17.26	17.11	23.46	15.31
Average value	58.76	34.46	23.44	5.20	10.81	10.94

Note: [0.05,0.1] represents the interval of loading rate between 0.05 and 0.1, m/s.

variation of the critical value with temperature is small. It shows that the changes in the micromechanical behavior of low-rank coals are mainly in the low-temperature stage, while the high-temperature stage is more stable.

- (4) The results of the sensitivity analysis of the micromechanical behavior show that smaller particle sizes have a greater effect on the cracks number, and larger particle sizes result in more pronounced variations in the peak stress. The variation in the ratio of mineral compositions has a significant effect on the cracks number, while it has no significant effect on the peak stress. A higher loading rate predicts a higher overall cracks number and peak stress.

CRediT authorship contribution statement

Jinglei Li: Writing – original draft, Software, Methodology, Conceptualization. **Haiyan Wang:** Writing – review & editing, Methodology, Funding acquisition, Conceptualization. **Haijie Yu:** Validation, Software. **Guobin Li:** Writing – review & editing, Supervision.

Declaration of competing interest

The authors declare that they have no known competing financial interests or personal relationships that could have appeared to influence the work reported in this paper.

Acknowledgments

The present work is supported by the National Key Research and Development Program of China(2023YFC3009101), the National Nature Science Foundation of China (51874313), the Major Science and Technology Program of Yazhou Bay Innovation Institute of Hainan Tropical Ocean University (2023CXYZD001), and the Research Project of Hainan Tropical Ocean University (RHDRC202330).

Data availability

Data will be made available on request.

References

- [1] B. Nie, X. Liu, L. Yang, J. Meng, X. Li, Pore structure characterization of different rank coals using gas adsorption and scanning electron microscopy, *Fuel* 158 (2015) 908–917.
- [2] Y. Cai, D. Liu, Z. Pan, Y. Yao, J. Li, Y. Qiu, Petrophysical characterization of Chinese coal cores with heat treatment by nuclear magnetic resonance, *Fuel* 108 (2013) 292–302.
- [3] G. Miao, Z. Li, L. Sun, Y. Yang, Experimental study on pore-fracture evolution law in the thermal damage process of coal, *Combust. Sci. Technol.* 116 (2019) 1–25.
- [4] Y. Tang, X. Zhong, G. Li, Z. Yang, G. Shi, Simulation of dynamic temperature evolution in an underground coal fire area based on an optimised Thermal-Hydraulic-Chemical model, *Combust. Theor. Model.* 23 (2018) 127–146.
- [5] S.T. Ide, F.M. Orr, Comparison of methods to estimate the rate of CO₂ emissions and coal consumption from a coal fire near Durango, CO, *International Journal of Coal Geology* 86 (2011) 95–107.
- [6] H. Li, B. Lin, Z. Chen, Y. Hong, C. Zheng, Evolution of coal petrophysical properties under microwave irradiation stimulation for different water saturation conditions, *Energy Fuels* 31 (2017) 8852–8864.
- [7] F. Xin, H. Xu, D. Tang, Y. Chen, L. Cao, Y. Yuan, Experimental study on the change of reservoir characteristics of different lithotypes of lignite after dehydration and improvement of seepage capacity, *Fuel* 277 (2020) 118196.
- [8] Y. Yao, D. Liu, Y. Che, D. Tang, S. Tang, W. Huang, Petrophysical characterization of coals by low-field nuclear magnetic resonance (NMR), *Fuel* 89 (2010) 1371–1380.
- [9] C. Su, J. Qiu, Q. Wu, L. Weng, Effects of high temperature on the microstructure and mechanical behavior of hard coal, *Int. J. Min. Sci. Technol.* 30 (2020) 643–650.
- [10] Y. Yang, K. Zheng, Z. Li, Z. Li, L. Si, S. Hou, Y. Duan, Experimental study on pore-fracture evolution law in the thermal damage process of coal, *Int. J. Rock Mech. Min. Sci.* 116 (2019) 13–24.
- [11] S. Liu, X. Li, D. Wang, M. Wu, G. Yin, M. Li, Mechanical and acoustic emission characteristics of coal at temperature impact, *Nat. Resour. Res.* 29 (2019) 1755–1772.

- [12] S. Liu, D. Wang, G. Yin, M. Li, X. Li, Experimental study on the microstructure evolution laws in coal seam affected by temperature impact, *Rock Mech. Rock Eng.* 53 (2019) 1359–1374.
- [13] C. Wang, M. He, X. Zhang, Z. Liu, T. Zhao, Temperature influence on macro-mechanics parameter of intact coal sample containing original gas from Baijiao Coal Mine in China, *Int. J. Min. Sci. Technol.* 23 (2013) 597–602.
- [14] W.-L. Tian, S.-Q. Yang, Y.-H. Huang, Macro and micro mechanics behavior of granite after heat treatment by cluster model in particle flow code, *Acta Mech. Sin.* 34 (2017) 175–186.
- [15] S.-Q. Yang, W.-L. Tian, Y.-H. Huang, Failure mechanical behavior of pre-holed granite specimens after elevated temperature treatment by particle flow code, *Geothermics* 72 (2018) 124–137.
- [16] Z. Zou, H. Tang, C. Xiong, A. Su, R.E. Criss, Kinetic characteristics of debris flows as exemplified by field investigations and discrete element simulation of the catastrophic Jiweishan rockslide, China, *Geomorphology* 295 (2017) 1–15.
- [17] Z. Xiang, T. Moon, J. Oh, X. Li, G. Si, I. Canbulat, Numerical investigation of borehole breakout and rock spalling based on strain energy criteria, *Int. J. Rock Mech. Min. Sci.* 171 (2023) 105587.
- [18] Z. Song, Z. Yang, M. Zhang, F. Wang, M. Herbst, H. Konietzky, Effect of heterogeneity on mechanical and micro-seismic behaviors of sandstone subjected to multi-level cyclic loading: a discrete element method investigation, *J. Rock Mech. Geotech. Eng.* 15 (2023) 2556–2581.
- [19] X. Ding, L. Zhang, H. Zhu, Q. Zhang, Effect of model scale and particle size distribution on PFC3D simulation results, *Rock Mech. Rock Eng.* 47 (2013) 2139–2156.
- [20] J. Deng, Q. Li, Y. Xiao, H. Wen, The effect of oxygen concentration on the non-isothermal combustion of coal, *Thermochim. Acta* 653 (2017) 106–115.
- [21] Q.-W. Li, Y. Xiao, C.-P. Wang, J. Deng, C.-M. Shu, Thermokinetic characteristics of coal spontaneous combustion based on thermogravimetric analysis, *Fuel* 250 (2019) 235–244.
- [22] X. Qi, Q. Li, H. Zhang, H. Xin, Thermodynamic characteristics of coal reaction under low oxygen concentration conditions, *J. Energy Inst.* 90 (2017) 544–555.
- [23] H. Wang, J. Li, X. Chen, C. Fan, P. Wang, L. Hu, Thermodynamic characteristics of oxidation and combustion of coal under lean-oxygen conditions, *ACS Omega* 6 (2021) 17255–17266.
- [24] Z. Tang, S. Yang, G. Wu, Occurrence mechanism and risk assessment of dynamic of coal and rock disasters in the low-temperature oxidation process of a coal-bed methane reservoir, *Energy Fuels* 31 (2017) 3602–3609.
- [25] L. Liu, M. Yang, X. Zhang, J. Mao, P. Chai, LNMR experimental study on the influence of gas pressure on methane adsorption law of middle-rank coal, *J. Nat. Gas Sci. Eng.* 91 (2021) 103949.
- [26] X. Zhang, B. Lin, Y. Li, C. Zhu, Q. Li, Analysis of fractal dimension of coal subjected to electrical breakdown based on nuclear magnetic resonance, *J. Nat. Gas Sci. Eng.* 79 (2020) 103345.
- [27] H. Wang, J. Li, Y. Zhang, Y. Wu, Z. Wang, Study on the evolution of the pore structure of low rank coal during spontaneous combustion, *Environ. Sci. Pollut. Control Ser.* (2023) 1–14.
- [28] S. Xie, H. Zhou, W. Jia, Y. Gu, Y. Cao, Z. Liu, Spatial evolution of pore and fracture structures in coal under unloading confining pressure: a stratified nuclear magnetic resonance approach, *Energy* 289 (2024) 130083.
- [29] H. Wang, J. Li, Z. Dong, C. Fan, Y. Zhang, X. Chen, Effect of thermal damage on the pore–fracture system during coal spontaneous combustion, *Fuel* 339 (2023) 127439.
- [30] S.-Q. Yang, Y.-H. Huang, Particle flow study on strength and meso-mechanism of Brazilian splitting test for jointed rock mass, *Acta Mech. Sin.* 30 (2014) 547–558.
- [31] Z. Xu, Z. Wang, W. Wang, P. Lin, J. Wu, An integrated parameter calibration method and sensitivity analysis of microparameters on mechanical behavior of transversely isotropic rocks, *Comput. Geotech.* 142 (2022) 104573.
- [32] S. Ji, J. Karlovsek, Optimized differential evolution algorithm for solving DEM material calibration problem, *Eng. Comput.* 39 (2022) 2001–2016.
- [33] S. Ji, J. Karlovsek, Calibration and uniqueness analysis of microparameters for DEM cohesive granular material, *Int. J. Min. Sci. Technol.* 32 (2022) 121–136.
- [34] H. Li, S. Shi, J. Lu, Q. Ye, Y. Lu, X. Zhu, Pore structure and multifractal analysis of coal subjected to microwave heating, *Powder Technol.* 346 (2019) 97–108.
- [35] L. Li, Y. Zhang, Y. Zhang, J. Sun, Z. Hao, The thermal activation process of coal gangue selected from Zhungeer in China, *J. Therm. Anal. Calorim.* 126 (2016) 1559–1566.
- [36] Q. Shi, B. Qin, Q. Bi, B. Qu, An experimental study on the effect of igneous intrusions on chemical structure and combustion characteristics of coal in Daxing Mine, China, *Fuel* 226 (2018) 307–315.
- [37] H. Wang, J. Li, C. Fan, L. Wang, X. Chen, Thermal kinetics of coal spontaneous combustion based on multiphase fully coupled fluid–mechanical porous media model, *Nat. Resour. Res.* 31 (2022) 2819–2837.
- [38] H. Li, C. Zheng, J. Lu, L. Tian, Y. Lu, Q. Ye, W. Luo, X. Zhu, Drying kinetics of coal under microwave irradiation based on a coupled electromagnetic, heat transfer and multiphase porous media model, *Fuel* 256 (2019) 115966.
- [39] Z. Pan, L.D. Connell, M. Camilleri, Laboratory characterisation of coal reservoir permeability for primary and enhanced coalbed methane recovery, *Int. J. Coal Geol.* 82 (2010) 252–261.
- [40] Y. Chu, D. Zhang, Study on the pore evolution law of anthracite coal under liquid nitrogen freeze-thaw cycles based on infrared thermal imaging and nuclear magnetic resonance, *Energy Sci. Eng.* 7 (2019) 3344–3354.
- [41] D.J. Xue, H.W. Zhou, Y.T. Liu, L.S. Deng, L. Zhang, Study of drainage and percolation of nitrogen–water flooding in tight coal by NMR imaging, *Rock Mech. Rock Eng.* 51 (2018) 3421–3437.
- [42] L. Weng, Z. Wu, Q. Liu, Z. Chu, S. Zhang, Evolutions of the unfrozen water content of saturated sandstones during freezing process and the freeze-induced damage characteristics, *Int. J. Rock Mech. Min. Sci.* 142 (2021) 104757.
- [43] Z. Liu, M. Zhang, S. Yu, L. Xin, G. Wang, L. Sun, Experimental study on the fractal features and permeability characteristics of low metamorphic coal pore structure under thermal damage, *Geofluids* 2020 (2020) 1–13.
- [44] C. Ren, B. Li, J. Xu, Y. Zhang, J. Li, Z. Gao, J. Yu, A novel damage-based permeability model for coal in the compaction and fracturing process under different temperature conditions, *Rock Mech. Rock Eng.* 53 (2020) 5697–5713.
- [45] H. Su, Q. Guo, H. Jing, L. Yu, J. Liu, Y. Gao, Mechanical performances and pore features of coal subjected to heat treatment in approximately vacuum environment, *Int. J. GeoMech.* 20 (2020) 06020011.
- [46] S.-Q. Yang, W.-L. Tian, P.G. Ranjith, Failure mechanical behavior of Australian strathbogie granite at high temperatures: insights from particle flow modeling, *Energies* 10 (2017) 756.
- [47] P. Guo, P. Zhang, M. Bu, H. Xing, M. He, Impact of cooling rate on mechanical properties and failure mechanism of sandstone under thermal–mechanical coupling effect, *International Journal of Coal Science & Technology* 10 (2023).
- [48] Y. Xu, B. Lin, Y. Li, Change laws of pore–fracture structure of coal under high-temperature steam shock, *ACS Omega* 7 (2022) 44298–44309.
- [49] F. Yang, Z. Ning, Q. Wang, R. Zhang, B.M. Krooss, Pore structure characteristics of lower Silurian shales in the southern Sichuan Basin, China: insights to pore development and gas storage mechanism, *Int. J. Coal Geol.* 156 (2016) 12–24.
- [50] A. Cao, G. Jing, Y.-l. Ding, S. Liu, Mining-induced static and dynamic loading rate effect on rock damage and acoustic emission characteristic under uniaxial compression, *Saf. Sci.* 116 (2019) 86–96.
- [51] B. Huang, J. Liu, The effect of loading rate on the behavior of samples composed of coal and rock, *Int. J. Rock Mech. Min. Sci.* 61 (2013) 23–30.
- [52] S. Okubo, K. Fukui, Q. Qingxin, Uniaxial compression and tension tests of anthracite and loading rate dependence of peak strength, *Int. J. Coal Geol.* 68 (2006) 196–204.